Short Hydrogen Bonds on Reconstructed Nanocrystal Surface Enhance Oxygen Evolution Activity

Jinlong Yang,[†] Jiaxin Zheng,[†] Ming Xu,[†] Zengqing Zhuo,[†,‡] Wanli Yang,[‡] Lin-Wang Wang,[§] Liming Dai,[⊥] Jun Lu,[¶] Khalil Amine,[¶] and Feng Pan[*,†]

[†]School of Advanced Materials, Peking University, Shenzhen Graduate School, Shenzhen 518055, People's Republic of China

[‡]Advanced Light Source, Lawrence Berkeley National Laboratory, Berkeley, California 94720, United States

[§]Materials Science Division, Lawrence Berkeley National Laboratory, Berkeley, California 94720, United States

[⊥]Department of Macromolecular Science and Engineering, Case Western Reserve University, 10900 Euclid Avenue, Cleveland, Ohio 44106, United States

[¶]Electrochemical Technology Program, Chemical Sciences and Engineering Division, Argonne National Laboratory, Argonne, Illinois 60439, United States

S *Supporting Information*

ABSTRACT: Water splitting to generate hydrogen and oxygen gas is critical to renewable energy technologies, including fuel cells and rechargeable metal−air batteries. The oxygen evolution reaction (OER) has long been the bottleneck of water splitting because of its high overpotential (η) and sluggish kinetics, and development of efficient, stable, and non-noble-metal-based OER catalysts has been an extensively studied topic. Here, we propose short hydrogen bonds on reconstructed nanocrystal surface to enhance oxygen evolution activity by investigating three types of phase structures (β_{II}, β_I, and γ_0) of Li_2CoSiO_4 (LCS) nanoparticles as OER electrocatalysts. Among them, the β_{II}-LCS outperforms the previously reported Co-based catalysts and the state-of-the-art IrO_2 catalyst for OER in the alkaline condition. Our experiments combined with ab initio calculations

indicated that due to the line-linked arrangement of Co active sites at the surface of β_{II}-LCS, short hydrogen bonds (2.54 Å) are formed and linked into a network at the reconstructed surface by rotating the flexible CoO_4 tetrahedra after surface delithiation, thus facilitating proton transfer and dissociation, leading to a unique dual-center catalytic pathway with low theoretical thermodynamic overpotential (0.35 eV) for the OER process.

KEYWORDS: β_{II}-Li_2CoSiO_4, nanocrystal surface, short hydrogen bond, proton transfer and dissociation, oxygen evolution activity
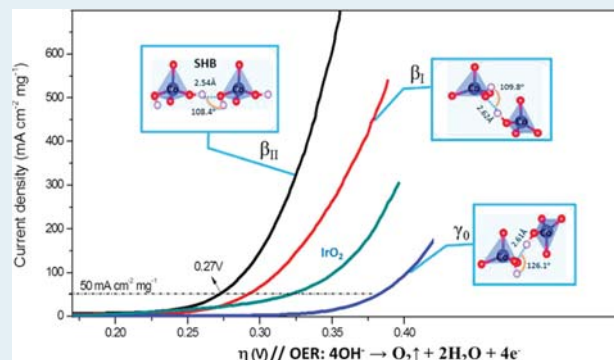
INTRODUCTION

To address the growing energy demand and the climate change problem, clean energy conversion and storage systems such as rechargeable metal−air batteries, water splitting devices, and fuel cells have attracted ever increasing interest.[1−3] The oxygen evolution reaction (OER), which is often associated with sluggish kinetics and high overpotential (η), is generally the rate-limiting step in the above systems.[4,5] Extensive efforts have been devoted to developing high-efficiency OER catalysts, particularly cheap alternative materials to the state-of-the-art noble-metal OER catalysts such as RuO_x and IrO_x. Over the last few decades, various 3d transition-metal (TM = Fe, Co, Ni, Mn, etc.) oxides and their derivatives have been widely studied as important alternative OER catalysts due to their earth-abundant, low cost, environmentally friendly features and high catalytic activity.[6−15] Among these catalytic materials, Co-based oxides and derivatives such as Co-based oxide nanocrystals,[6,7] sulfides,[8] selenides,[9] phosphides,[10] nitrides,[11] borides,[12] perov-

skites,[13] and layered hydroxide[14,15] are stable and have been proven to be highly competitive with noble-metal catalysts.

OER is a four-electron process which involves the H_2O or OH^- reactants adsorption, O−H bond breaking, O=O double bond formation, O_2 product dissociation, and the coupling of multiple proton and electron transfers.[4,5] The catalytic activity of OER catalysts is closely associated with the numbers and the intrinsic activity of the OER active sites, namely the TM atoms at the surfaces of the catalysts. The numbers of the surface active sites generally depend on the morphology and size of the catalysts. Thus, nano- and porous-structures with large specific surface area were usually designed to enhance the catalytic activity.[8] The intrinsic activity of the TM active site is highly related to the electronic structures (spin configuration and
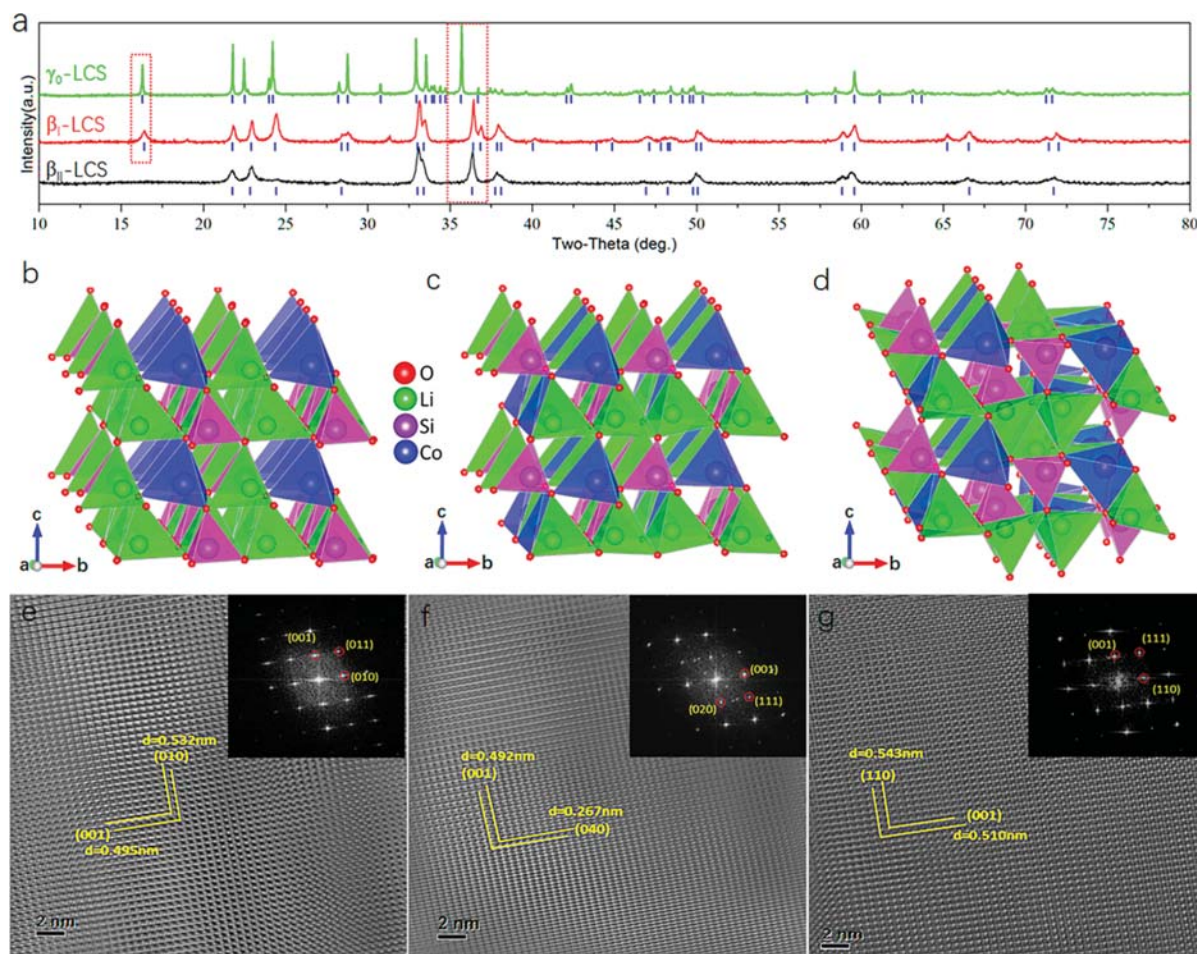
Figure 1. (a) XRD patterns of the β_{II}-, β_{I}-, and γ_{0}-LCS nanocrystals, obtained at low temperature of 200 °C, moderate heating temperature of 700 °C, and high temperature of 1100 °C and then quenched from 850 °C, respectively. Schematic presentations of (b) β_{II}-, (c) β_{I}-, and (d) γ_{0}-LCS structures. HRTEM images of three LCS phases: (e) β_{II}, (f) β_{I}, and (g) γ_{0}. Insets in every HRTEM images are the corresponding selected-area electron-diffraction pattern (top right corner).

oxidation state) of surface TM ions and their local coordination environments. For example, Shao-Horn and coworkers[13] demonstrated that the OER activity of perovskite oxides directly depends on the e_g orbital filling of the transition-metal ions, which is named as Shao-Horn's principle. In addition, Liu et al.[16] investigated the geometrical site-dependent OER activity of spinel Co_3O_4 catalyst by substituting Co^{2+}_{Td} and Co^{3+}_{Oh} with inactive Zn^{2+} and Al^{3+}, demonstrating that Co^{2+}_{Td} site is responsible for the formation of cobalt oxyhydroxide (CoOOH), which acts as the active site for water oxidation. Cui and coworkers[17,18] recently reported that the OER activity of $LiCoO_2$ and $LiCoPO_4$ was remarkably enhanced by tuning the Co oxidation state via electrochemical delithiation process. More interestingly, Kim et al.[19] selected four cobalt-based phosphate catalysts ($Li_2CoP_2O_7$, $LiCoPO_4$, $Na_2CoP_2O_7$, and $NaCoPO_4$) with various cobalt- and phosphate-group coordination and proved the importance of local cobalt coordination in the catalysis. Density functional theory calculations revealed that $Na_2CoP_2O_7$ four- and five-coordinated cobalt atoms have lower theoretical η (~0.42 eV) compared with the most active cobalt oxide phase CoOOH (~0.48 eV), theoretically verifying its high catalytic activity and suggesting the possible effect of polyanions on the water splitting.

One of the critical steps for OER is the breakup of the O–H bond at the surface of the catalyst. A hydrogen bond between two O atoms via a center H atom can facilitate such O–H bond breaking when the hydrogen bonds become short. Indeed, short hydrogen bonds (SHB) are employed for the acceleration of a wide range of chemical processes in biological catalysis and small-molecule synthetic catalysis, leading to a low barrier for O–H bond breaking.[20] Previous OER studies also reported the existence of surface hydrogen bonds $O_s\cdots H-O_{ad}$ (O_s and O_{ad} denote the surface oxygen atom of transition-metal oxides and the oxygen atom of the adsorbed hydroxyl group or water molecule without bonding to transition metals, respectively) and their roles in O–H bond breaking during the water splitting.[21] In this context, we postulated that a short hydrogen bond between two surface O atoms bonded with transition metals can potentially play an important role in OER.

Inspired by the above thoughts, we synthesized three types of phase structures (β_{II}, β_{I}, and γ_{0}) of Li_2CoSiO_4 (LCS) nanoparticles. The same case is that the three structures all consist of CoO_4, SiO_4, and LiO_4 to create tetrahedral networks with point connection, leading to flexibly tuning tetrahedral during delithiation. Using them as OER electrocatalysts for water splitting, β_{II}-LCS was found to show the highest catalyst activity, outperforming the state-of-the-art IrO_2 as well as all the
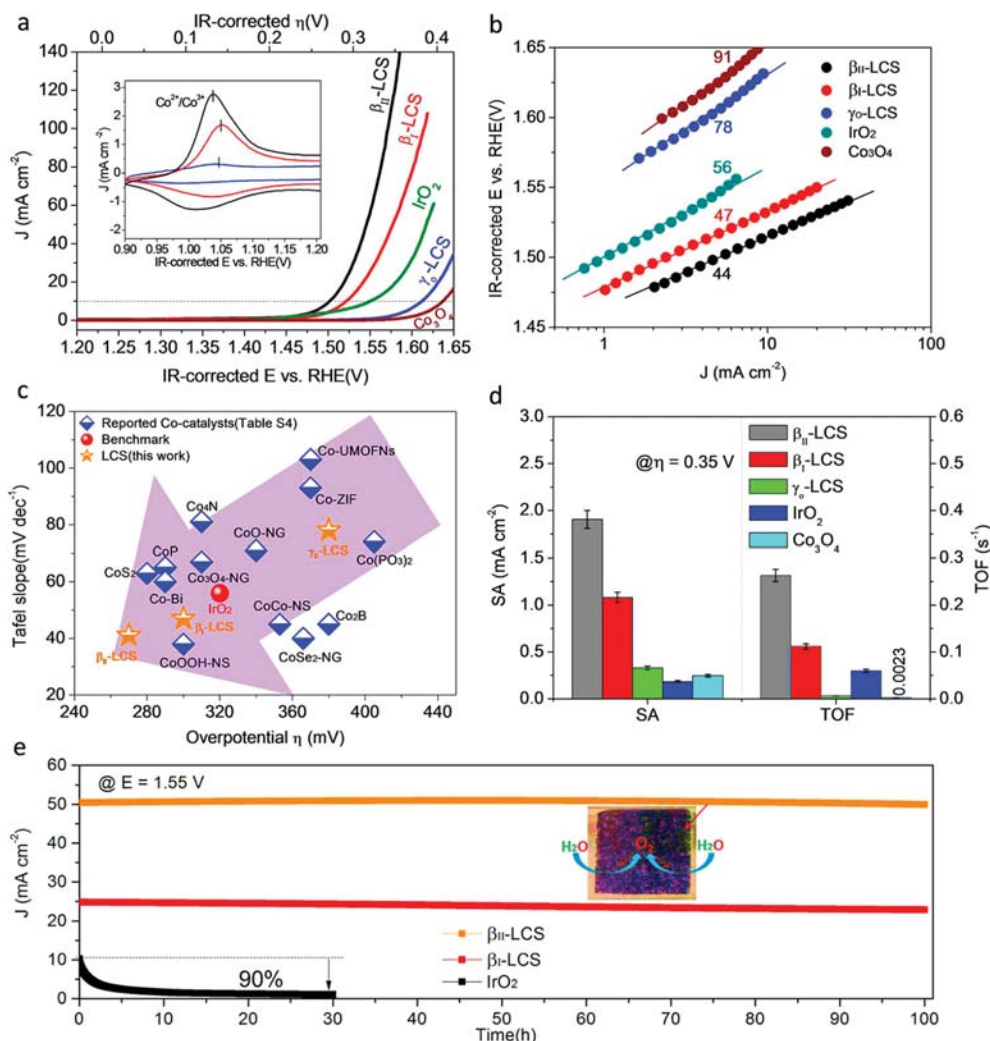
Figure 2. (a) Polarization curves and (b) Tafel plots for the OER on the RDE (1600 rpm) consisting of the β_{II}-, β_I-, and γ_0-LCS samples, benchmarked IrO_2, and Co_3O_4 catalysts in O_2-saturated 1 M KOH solution (scan rate: 10 mV s^{-1}). (c) OER activity comparison graph showing η = 10 mA cm^{-2} and Tafel slopes for Co-based catalysts reported in the last three years. (d) SA normalized to real surface area and TOF assuming every metal atom to be catalytically active. (e) Chronoamperometry ($J-t$) of the LCS series (β_{II}-LCS and β_I-LCS) and IrO_2 catalysts loaded onto carbon fiber paper moderated at 1.55 V (corresponding to η = 0.32 V that delivered ~10 mA cm^{-2} for IrO_2).

RESULTS AND DISCUSSION

Lithium transition-metal silicates (Li_2MSiO_4, M = Fe, Co, Ni, and Mn), a large family of tetrahedral structured materials, are known as transition-metal redox-active electrode materials in rechargeable lithium-ion batteries.[22,23] In their structures, each transition metal, lithium, and silicon are surrounded by four oxygen atoms, and the MO_4 tetrahedra are cross-linked by silicate groups and flexibly tuned during surface delithiation in Li_2MSiO_4. These are different from the full octahedron (e.g., layered $LiMO_2$) and octahedron/tetrahedron hybrid structures

previously reported Co-based catalysts. Our experimental results and ab initio calculations confirmed that with the extraction of the surface lithium ions, short hydrogen bonds (2.54 Å) formed on the reconstructed nanocrystal surface of β_{II}-LCS by rotating of the flexible CoO_4 tetrahedra to facilitate proton transfer and dissociation, leading to a unique dual-center catalytic OER pathway with low-energy barriers (0.35 eV). These findings offer a new guideline to designing efficient OER catalysts.

(e.g., olivine $LiMPO_4$ and spinel structures). Interestingly, these tetrahedral structures exhibit a rich polymorphism[24] which depends on the synthesized condition. Their different atomic structures and arrangements, particularly on the surface under the electrochemical operating conditions, would lead to different electrocatalytic activities for OER.

To validate this hypothesis, three LCS polymorphic nanocrystals were selected as OER electrocatalysts. These LCS nanocrystals were synthesized by a precise temperature control method (see the Supporting Information for detailed synthesis). From the powder X-ray diffraction patterns (Figure 1a), it can be seen that all the diffraction peaks of LCS obtained at low temperature (200 °C) are consistent with the standard pattern of the reported orthorhombic β_{II} structural LCS with Pmn2$_1$ space group.[23] When the β_{II}-LCS was heated in air to 700 °C, a single reflection around 2θ = 16.4° appeared, corresponding to the (011) plane of orthorhombic β_I structural LCS with Pbn2$_1$ space group (S.G.).[23] Following the study by Bruce and coworkers,[24] the monoclinic γ_0-LCS with P2$_1$/n S.G. was formed by heating β_I-LCS to 1100 °C then quenching from
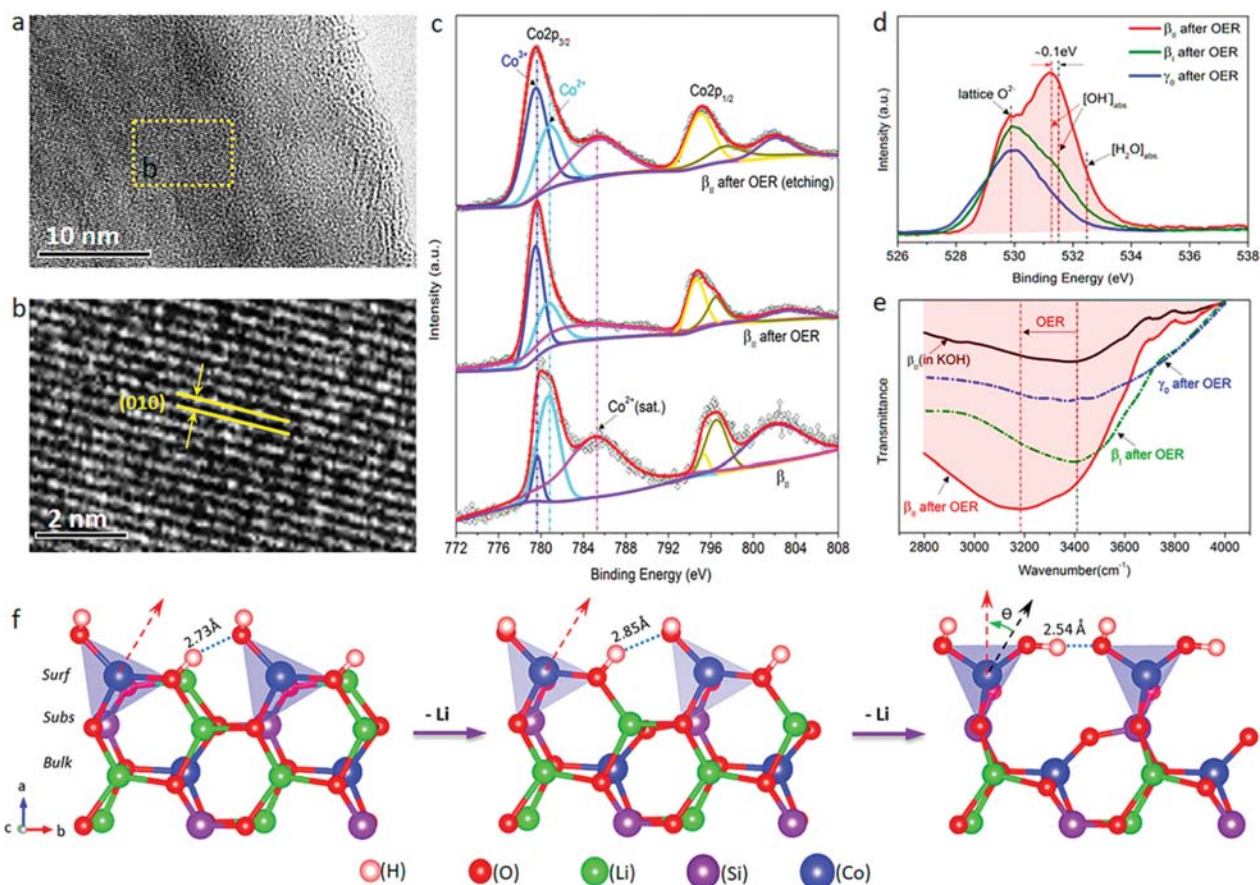
Figure 3. (a) HRTEM image and (b) internal lattice fringes of β_{II}-LCS nanocrystal after OER (1.55 V). (c) XPS spectra of Co 2p in the β_{II}-, β_{I}-, and γ_0-LCS samples after OER (1.55 V). (d) Three characteristic peaks at binding energy of O 1s: ≈532.5 eV for surface adsorbed H_2O groups on Co active sites $[H_2O]_{ads.}$, ≈529.6 eV for lattice O^{2-} referenced to pure β_{II}-LCS, and ≈531.5 eV for surface adsorbed OH groups on Co active sites $[OH^-]_{ads.}$. (e) ATR-FTIR related to H–O bond bending and stretching. (f) Structure evolution of (100) surface of β_{II}-LCS with the surface lithium extracted and the formation process of SHB during delithiation. Surf, subs, and bulk refer to the surface, subsurface, and bulk of the β_{II}-LCS, respectively.

850 °C, featuring the 100% intensity of reflection at $2\theta = 35.7°$ corresponding to its (002) plane. Figure S1 shows the Rietveld refinement of the X-ray diffraction data for the three phases of LCS nanocrystals. The observed and calculated patterns match well with each other. The structural parameters obtained from the Rietveld refinement are shown in Tables S1−3. The local nanocrystal structure of β_{II}-, β_{I}-, and γ_0-LCS along with the lattice parameters based on Rietveld analysis are shown in Figures 1b−d, respectively. In β_{II} phase, all CoO_4, SiO_4, and LiO_4 tetrahedra point in the same direction, perpendicular to the close-packed planes, and CoO_4 tetrahedra link into several active lines along the a-axis direction by vertex oxygen; compared to those in the β_{II} phase, the active lines in β_{I} phase are broken, and CoO_4 tetrahedra are isolated due to the exchange of partial cobalt and lithium sites. In γ_0 phase, besides the exchange of partial cobalt and lithium sites, half of the tetrahedra point in the direction opposite to the other half.

The surface morphologies of the β_{II}-, β_{I}-, and γ_0-LCS nanocrystals were examined by scanning electron microscopy (SEM) and transmission electron microscopy (TEM) images. It can be observed from Figure S2 that the length and width of β_{II}-LCS nanoparticles are ∼100 and ∼50 nm, respectively, and the moderate heating temperature of 700 °C cannot change the size of the β_{I}-LCS nanoparticles but the higher temperature at 1100 °C makes the γ_0-LCS particles into larger micron chunks,

also reflected from the decreased specific surface area (Figure S3). High resolution transmission electron microscopy (HRTEM) images in Figures 1e−g further show that the (100) normal surfaces are the main exposed surfaces for the three phases. Our previous simulated equilibrium crystal morphologies[25] of the β_{II}-, β_{I}-, and γ_0-LCS structures via ab initio calculations combined with Wulff constructions also showed that the (100) normal surfaces are the main exposed surfaces for the three phases (see more details in the insets of Figures S2g−i, Section S2.1, and ref 25), indicating the observed (100) surfaces in HRTEM images of three phases are the energy favorable surfaces. In addition, the accurate d spacing value for ⟨100⟩ zone axes in HRTEM images (Figures 1e−g) and corresponding selected-area electron diffraction (SAED) patterns (inset in Figures 1e−g) further confirm the three phase structures. X-ray photoelectron spectroscopy (XPS) analysis (Figure S4) shows the valence state of cobalt on the surfaces of the three structures is all 2+. Therefore, the active sites in the three structures are all Co^{2+}_{Td} with coordination of CoO_4, stabilized by SiO_4 and LiO_4 tetrahedral networks. The arrangement and orientation of the CoO_4, SiO_4, and LiO_4 tetrahedra in the three structures are different, which would affect their catalytic activities for OER directly.

The catalytic OER activities of LCS series were evaluated by linear sweep voltammetry (LSV) in O_2-saturated 1 M KOH

using a typical thin-film rotating disk electrode (RDE) technique.[14,15] As a reference, similar measurements were performed on conventional Co_3O_4 and benchmark IrO_2 catalysts. In Figure 2a, the LSV curves with IR-correction show that all LCS catalysts have a much lower onset potential and higher catalytic current than those of Co_3O_4. In addition, the OER currents of β_{II}-LCS and β_{I}-LCS exceed that of IrO_2 significantly, despite the slightly lower onset potential of IrO_2 (~1.45 V, with a very weak and slow onset). It is more meaningful to compare the relative values (η_{10}) of the η required to achieve a current density of 10 mA cm^{-2}, which is a metric relevant to solar fuel synthesis.[7] The η_{10} values for β_{II}-, β_{I}-, and γ_0-LCS were approximately 270, 300, and 380 mV, respectively. Remarkably, the η_{10} values of β_{II}- and β_{I}-LCS catalyst are much smaller than the best values of IrO_2 (330 mV) reported in previous works.[7,15] From the Tafel plots (an important factor for the evaluation of OER kinetics) in Figure 2b, we can see that the Tafel slopes of β_{II}-LCS, β_{I}-LCS, and γ_0-LCS are approximately 44, 47, and 78 mV decade^{-1}, respectively. The Tafel slopes for β_{II}- and β_{I}-LCS are also much smaller than that for the benchmark IrO_2 catalysts (56 mV decade^{-1}, this value is also among the best reported values for IrO_2[7,15]). Thus, the β-series LCS catalysts are superior to the current state-of-the-art OER catalysts. Figure 2c shows a comparison for the catalytic activity (η_{10} values) and kinetics (Tafel slopes) of the LCS series with previously reported Co-based OER electrocatalysts (Table S4 shows the detailed values). Among all the reported Co-based catalysts, Co_3O_4–NG,[7] Co_3N,[11] CoP,[10] CoS_2,[8] Co–Bi,[26] and CoOOH-NS[14] present a lower η_{10} than that of the benchmark IrO_2 catalyst. $CoSe_2$,[9] CoCo-NS,[15] Co_2B,[12] and CoOOH-NS show better kinetics than does benchmark IrO_2. It is easy to observe that only β_{II}-LCS, β_{I}-LCS, and the reported CoOOH-NS engage both advantages for catalytic activity and kinetics, and the β_{II}-LCS catalyst remains one of the best OER catalysts. In view of the use of multiple transition-metal doping to enhance OER activities,[15,26,27] the activity of β_{II}-LCS is anticipated to be further improved by generating multi-TM-doped β_{II}-LCS.

We then calculated the turnover frequency (TOF) and specific activity (SA) of the LCS series nanocatalysts to compare the intrinsic OER performance. The TOF reveals the activities of the above catalysts when assuming every metal atom to be catalytically active, and the SA is normalized to the specific surface area (Figure S3) and reflects the intrinsic activity of a catalyst.[14,15] As shown in Figure 2d, the β_{II}-LCS catalyst exhibits the highest TOF of ~0.27 s^{-1} at η = 350 mV, which is ~2.5, 5.0, 41, and 111 times, respectively, higher than that of β_{I}-LCS, IrO_2, γ_0-LCS, and Co_3O_4 catalysts at identical conditions. Consistent with the TOF results, the SAs of the LCS series at η = 350 mV are much higher than those of Co_3O_4 and IrO_2, and β_{II}-LCS has the highest SA value of 1.85 mA cm^{-2}. Thus, β_{II}-LCS shows a high intrinsic OER activity.

Using IrO_2 as the reference, chronopotentiometry ($E-t$) measurements were finally performed with a glassy carbon electrode to evaluate the catalytic long-term durability for the LCS catalysts. As shown in Figure S5, the β_{II}-, β_{I}-, and γ_0-LCS retained nearly a constant operating potential of 1.5, 1.53, and 1.61 V, respectively, for delivering 10 mA cm^{-2} current density at a pH value of 14 over an operation time of 10 000 s, whereas the potential of IrO_2 increased steadily (>60 mV) under the same conditions. Moreover, chronoamperometry ($J-t$) of the LCS series catalysts loaded onto a carbon fiber paper (CFP) under a potential of E = 1.55 V (corresponding to η = 320 mV

that delivered ~10 mA cm^{-2} current density for the benchmark IrO_2) also shows excellent stability over 100 h (Figure 2e). Clearly, the β_{II}-LCS catalyst can deliver an ultrahigh activity and excellent durability and holds great potential as an efficient, robust, and cost-effective OER catalyst of practical significance.

HRTEM was first employed to evaluate the structural evolution of the β_{II}-, β_{I}-, and γ_0-LCS samples after chronoamperometry for 20 h at +1.55 V vs RHE in the OER region. In β_{II}- and β_{I}-LCS samples, the periodicity of the crystals (Figure 3a and S6) is reduced on the surface of ~10 nm depth, but the internal lattice (Figure 3b) fringes are intact, illustrating that the surface structural changes occur in both β_{II}- and β_{I}-LCS samples with ~10 nm depth during OER. In γ_0-LCS sample (Figure S6), surface structural changes occur only at atomic layer depth on the surface. In view of lithium-ion battery electrode materials as OER catalysts, the oxidation reaction on the surface of β_{II}- and β_{I}-LCS catalysts was accompanied by delithiation in the electrochemical environment.[17] Ab initio calculated results (see Section S2.2 for detailed calculations) show that the surface and subsurface voltages of delithiation in β_{II}- and β_{I}-LCS catalysts are consistent with the oxidation peaks around 1.0 V in tested LSV curves (Figure 2a, inset), which are lower than the bulk values. It is most likely that the Li ions at the surface and subsurface were fully extracted while the bulk lithium atoms were partially extracted due to the poor lithium ion diffusion of the full tetrahedron orthosilicates.[22,28] Nevertheless, the delithiation peak around 1.0 V of γ_0-LCS is too weak to be ignored, indicating that its delithiation on the surface is difficult.

XPS further demonstrates that the delithiation occurs only at the surface of the β_{II}- and β_{I}-LCS. Before OER, the binding energies of Li 1s in 3 LCS samples locate at 54.9 eV, and the binding energy of Co 2p3/2 at 780.8 eV corresponds Co^{2+} (Figure S4); after OER, XPS in Figure S7 shows that Li signal of the β_{II}- and β_{I}-LCS samples were lacking, and the broad peaks at Co 2p3/2 are consistent with the fitting results of Co^{2+} ($2p_{3/2}$ at 780.8 eV) and Co^{3+} ($2p_{3/2}$ at 779.5 eV).[7] The ratio of Co^{3+}/Co^{2+} follows the order of $\beta_{II} \approx \beta_{I} > \gamma_0$. The results from synchrotron-based surface sensitive soft X-ray absorption spectroscopy (sXAS) further confirm this conclusion (Figure S8). Subsequently, we employed argon ions to etch the surface of the catalysts for 50 s to obtain the element information inside the crystal. The results (Figure 3c) show that Co 2p in etching LCS sample has the same satellite at 785.5 eV as LCS before OER. This satellite represents the characteristics of Co^{2+} and further supports the unchanged internal structure of LCS after OER. Therefore, XPS experiment results provided evidence for the stability of the surface delithiated LCS particles. In addition, it has been reported that lithium transition-metal silicate materials have stable delithiated structures,[22,29,30] which revealed the stability of the delithiated LCS particles. Therefore, we believed that the surface delithiated LCS particles in 1 M KOH electrolyte are very similar to transition-metal phosphide (MP)[31,32] catalysts for water splitting, all of which have oxidation on the surface of catalytic particles with unchanged internal structure and show long-term stability for OER.

What factors account for the high intrinsic activity of β_{II}-LCS nanocrystal for OER? We investigated the O 1s binding energy on the surfaces of the β_{II}-, β_{I}-, and γ_0-LCS before and after OER (Figure S4c and Figure 3d). The binding energy at 529.8 eV belongs to the lattice O^{2-} referenced to LCS nanocrystal, and 532.5 and 531.5 eV correspond to the adsorbed molecular
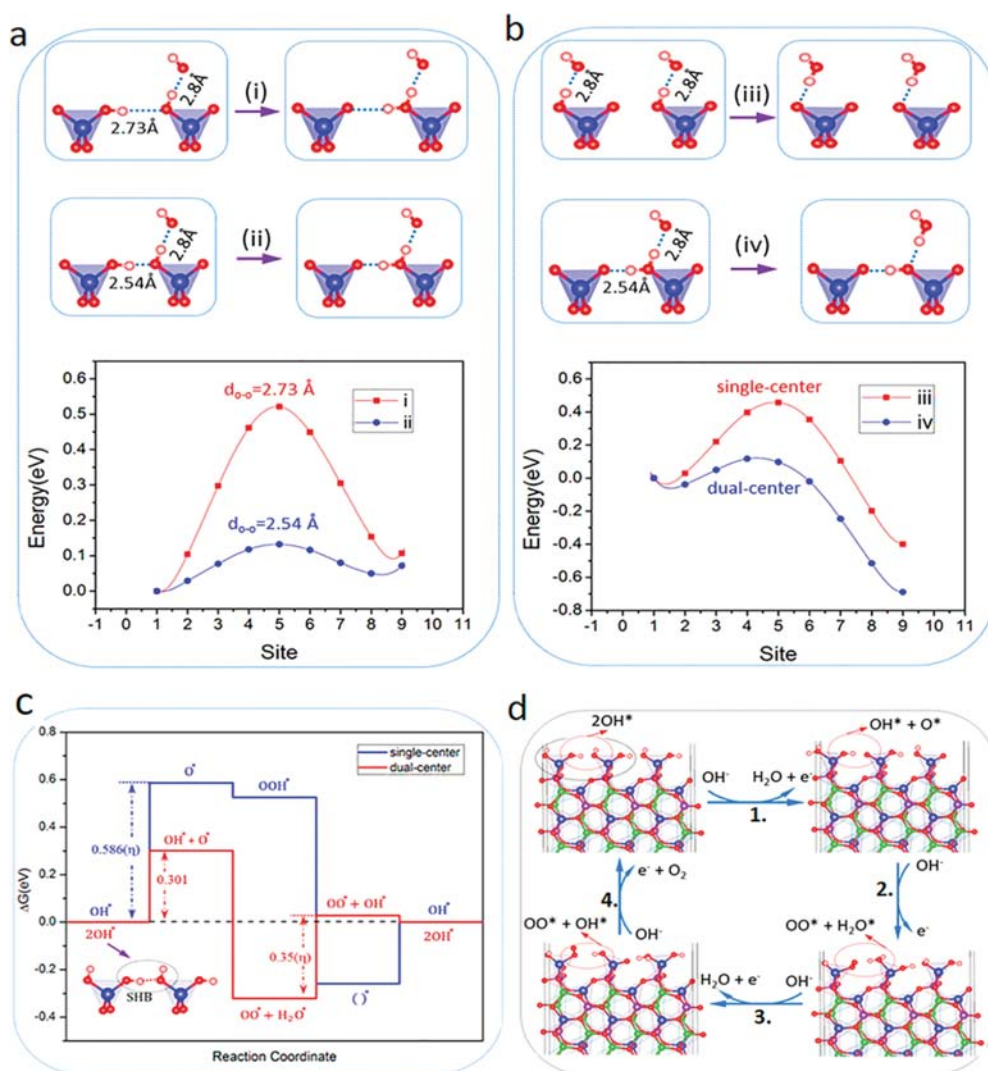
Figure 4. (a) Proton transfer between two OH adsorbed on the (100) face of β_{II}-LCS under alkaline conditions and corresponding energy barriers (i) before delithiation with longer hydrogen bond and (ii) after delithiation with SHB of 2.54 Å. (b) Proton dissociation step and its corresponding energy barrier between one chemisorbed OH* and one adjacent OH$^-$ in the alkaline solution in the OER process (the hydrogen bond between such two OH$^-$ is fixed with length of 2.8 Å): (iii) single-center model without SHB and (iv) dual-center model with SHB of 2.54 Å after proton transfer along the SHB. (c) Free-energy landscape of dual- and single-center models and (d) dual-center route with SHB on the (100) surface of delithiated β_{II}-LCS.

water $[H_2O]_{ads}$ and hydroxyl $[OH^-]_{ads}$, respectively.[33,34] Interestingly, the binding energy of $[OH^-]_{ads}$ for β_{II}-LCS after OER shifts negative about 0.1 eV, meaning a stretch of O–H bonds in the OER process. Fourier transform infrared spectroscopy (FTIR) with attenuated total reflection (ATR) was used to further probe the O–H bonds. We are interested in the phonon modes related to H–O stretching at about 3400 cm^{-1}, which do not overlap with other phonon modes. Before OER, all the three-phased LCS catalysts exhibit O–H stretching peaks at about 3400 cm^{-1} of pure water (Figure S9), the strongest O–H stretching peak of β_{II}-LCS nanocrystal indicates the most OH adsorption.[35] After OER catalysis, the OH$^-$ adsorption capacities of all LCS nanocrystals further increase, but only the FTIR peak for the β_{II} phase shifted to even lower wavenumbers of 3200 cm^{-1} (Figure 3e). It is well-known that a saturated H bond (e.g., the SHB) shows a softer H vibration mode.[36] Thus, the observed reduction in the FTIR

peak wavenumber after OER agrees with the formation of SHB, leading to the binding energy of OH$_{abs}$ being shifted negatively.

On the basis of above results, we computed OH adsorption on the delithiated structures for the three phases in alkaline media using ab initio calculations (Figure S10). Interestingly, we found that hydrogen bonds are indeed formed between two adjacent OH$^-$ groups, which are chemisorbed on two adjacent Co atoms on the delithiated (100) surface of β_{II}-LCS. Figure 3f shows the calculated structure evolution with the surface lithium extraction for the (100) surface of β_{II}-LCS with OH adsorption. The calculated surface Pourbaix diagram based on the (100) face of β_{II}-LCS after and before the delithiation (Figure S11) proves that the adsorption structures in Figure 3e are the most stable structures without the external voltage within the range of pH 0–14. As reported by our previous work,[22] due to the vertex-connected tetrahedron network of LMS (M = Fe, Co, and Mn), a large structural distortion occurs during the lithium extraction, leading to surface reconstruction

and rotation for the MO_4 tetrahedron. Compared to the $LiCoO_2$ with a hard framework of the CoO_6 octahedron, the tetrahedral structures of LCS are flexible and soft and thus can be easily manipulated during delithiation. Because of this flexibility, the hydrogen bond distance (d_{o-o}) first increases from 2.73 to 2.85 Å with the surface lithium extraction and then decreases to 2.54 Å with the subsurface further lithium extraction, corresponding to the SHB with lower FTIR peak and negatively shifted binding energy. Nevertheless, the d_{o-o} on the delithiated surface (see Section S2.4 for detailed calculations) of β_I and γ_0 phase is much longer at 2.62 and 2.61 Å, respectively. The calculated results (Tables S9−11) show that short hydrogen bonds on delithiated surface of β_{II}-LCS possess a higher possibility than those of β_I- and γ_0-LCS, which is attributed to the line-linked arrangement of Co^{2+}_{Td} active sites (indicating a short distance between two adjacent Co active sites (Figure 1b)) in the β_{II} structure. We proposed that the 2.54 Å of SHB could link into a network on the reconstructed surfaces of β_{II}-LCS and was the main reason for the high OER activity and kinetics.

The possible effects of a SHB on the proton transfer (see Section S2.5 for detailed calculations) were calculated. Figure 4a shows the calculated energy barriers for the proton transfer between two OH^- ions adsorbed on two adjacent Co ions on the surface without delithiation (image i: hydrogen bond of 2.725 Å) and with full delithiation (image ii: short hydrogen bond of 2.54 Å). These data indicate that the proton transfer exhibits a much lower energy barrier between the two adsorbed OH^- ions to generate an SHB. Figure 4b shows the calculated energy barriers for the proton dissociation step of the OER process in the single-center model (image iii: one OH^- is adsorbed on one Co without SHB at the surface) and dual-center model (image iv: two OH^- ions are adsorbed on two adjacent Co ions on the surface to generate the SHB). It was found that, compared with the proton dissociation step in the single-center model (image iii: barrier of 0.45 eV), the short hydrogen bond in the dual-center model makes the proton dissociation much easier for the OH adsorbed on the Co (image iv: barrier of 0.11 eV). Thus, the combined route ii and iv with the SHB based dual-center model is the energy preferential path for proton transfer, O−H bond breakage, and faster reaction kinetics.

On the basis of the above analysis, we propose an SHB dual-center model for the β_{II}-LCS OER nanocatalysts (see Section S2.6 for detailed calculations). Figure 4c shows the free-energy landscape of the β_{II} phase for a single- and dual-center model at pH 14 and a voltage of 1.23 V. We can see that for the β_{II}-LCS, the first proton dissociation (OH* to O*) is the potential-limiting step for the single-center model with a much higher η of 0.586 V, whereas the free energy change of the first proton dissociation (step 1) is 0.3 eV for the dual-center model, and the third proton dissociation (from OO* + H_2O* to OO* + OH*) is the potential-limiting step in the dual-center model with η of 0.35 V, which is lower than the theoretical values of β_I- (Figure S17) and γ_0- (Figure S18) LCS as well as the recently reported CoOOH-NS (0.48 eV).[14] Thus, the SHB in β_{II}-LCS decreases the proton dissociation energy significantly, leading to a lower η. Figure 4d shows the detailed dual-center route on the (100) surface of β_{II}-LCS for OER. Although the proposed dual-center reaction path with the SHB is a more efficient way for the OER catalyst, the possible effect of the single-center model cannot be ruled out. It is most probably the single- and dual-center models working together in the OER

process. According to the above theoretical prediction, the β_{II}-LCS should have a high OER catalyst activity and kinetics for water splitting.

CONCLUSION

In summary, three phases (β_{II}, β_I, and γ_0) of LCS nanocrystals were investigated as OER electrocatalyst for water splitting in alkaline media. The β_{II}-LCS was proven to be a highly efficient, robust, and cost-effective OER electrocatalyst, outperforming IrO_2 and most reported Co-based catalysts in recent years. Our experiments combined with ab initio calculations indicated that due to the line-linked arrangement of Co^{2+}_{Td} active sites at the surface of β_{II}-LCS, short hydrogen bonds are formed on the delithiated surface of β_{II}-LCS by surface reconstruction and rotation of the flexible CoO_4 tetrahedron, which contributed significantly to the OER by facilitating proton transfer. Our findings emphasize the importance of SHB in catalysis. We expect that this result will broaden the current scope to design highly efficient OER catalysts for water splitting.

ASSOCIATED CONTENT

ⓢ Supporting Information

The Supporting Information is available free of charge on the ACS Publications website at DOI: 10.1021/acscatal.7b02814.

> Experimental details; refined XRD, FTIR, SEM, TEM, BET, XPS, sXAS, and chronopotentiometry ($E−t$) results of the LCS series; ab initio calculations, including surface Wulff constructions, delithiation structures, and Pourbaix diagram; energy barrier of proton transfer and dissociation; OER reaction coordinates; and Gibbs free energy based on short hydrogen bonds (PDF)

AUTHOR INFORMATION

Corresponding Author
*E-mail: panfeng@pkusz.edu.cn.

ORCID ⓘ
Wanli Yang: 0000-0003-0666-8063
Jun Lu: 0000-0003-0858-8577
Khalil Amine: 0000-0001-9206-3719
Feng Pan: 0000-0002-8216-1339

Author Contributions
J.Y., J.Z., and M.X. contributed equally to this work. F.P., J.Y., and J.Z. designed the project. J.Y. performed the catalyst preparation and tests; M.X., J.Z., and L.W. performed the ab initio calculations, and Z.Z. and W.Y. carried out measurements and data analyses. J.Y., J.Z., M.X., J.L., K.A., L.D., and F.P. discussed the results, analyzed the data, and drafted the manuscript. All authors reviewed the manuscript.

Notes
The authors declare no competing financial interest.

ACKNOWLEDGMENTS

■ REFERENCES

(1) Gratzel, M. *Nature* **2001**, *414*, 338−344.

(2) Zhang, M.; de Respinis, M.; Frei, H. *Nat. Chem.* **2014**, *6*, 362−367.

(3) Kim, T. W.; Choi, K. S. *Science* **2014**, *343*, 990−994.

(4) Oh, S. H.; Black, R.; Pomerantseva, E.; Lee, J. H.; Nazar, L. F. *Nat. Chem.* **2012**, *4*, 1004−1010.

(5) Kanan, M. W.; Nocera, D. G. *Science* **2008**, *321*, 1072−1075.

(6) Liang, Y. Y.; Li, Y. G.; Wang, H. L.; Zhou, J. G.; Wang, J.; Regier, T.; Dai, H. *Nat. Mater.* **2011**, *10*, 780−786.

(7) Ma, T. Y.; Dai, S.; Jaroniec, M.; Qiao, S. Z. *J. Am. Chem. Soc.* **2014**, *136*, 13925−13931.

(8) Chen, W.; Liu, Y. Y.; Li, Y. Z.; Sun, J.; Qiu, Y. C.; Liu, C.; Zhou, G. M.; Cui, Y. *Nano Lett.* **2016**, *16*, 7588−7596.

(9) Gao, M. R.; Cao, X.; Gao, Q.; Xu, Y. F.; Zheng, Y. R.; Jiang, J.; Yu, S. H. *ACS Nano* **2014**, *8*, 3970−3978.

(10) Yang, Y.; Fei, H. L.; Ruan, G. D.; Tour, J. M. *Adv. Mater.* **2015**, *27*, 3175−3180.

(11) Meng, F. L.; Zhong, H. X.; Bao, D.; Yan, J. M.; Zhang, X. B. *J. Am. Chem. Soc.* **2016**, *138*, 10226−10231.

(12) Masa, J.; Weide, P.; Peeters, D.; Sinev, I.; Xia, W.; Sun, Z. Y.; Somsen, C.; Muhler, M.; Schuhmann, W. *Adv. Energy Mater.* **2016**, *6*, 1502313.

(13) Suntivich, J.; May, K. J.; Gasteiger, H. A.; Goodenough, J. B.; Shao-Horn, Y. *Science* **2011**, *334*, 1383−1385.

(14) Huang, J. H.; Chen, J. T.; Yao, T.; He, J. F.; Jiang, S.; Sun, Z. H.; Liu, Q. H.; Cheng, W. R.; Hu, F. C.; Jiang, Y.; Pan, Z. Y.; Wei, S. Q. *Angew. Chem., Int. Ed.* **2015**, *54*, 8722−8727.

(15) Song, F.; Hu, X. L. *Nat. Commun.* **2014**, *5*, 1.

(16) Wang, H. Y.; Hung, S. F.; Chen, H. Y.; Chan, T. S.; Chen, H. M.; Liu, B. *J. Am. Chem. Soc.* **2016**, *138*, 36−39.

(17) Liu, Y. Y.; Wang, H. T.; Lin, D. C.; Liu, C.; Hsu, P. C.; Liu, W.; Chen, W.; Cui, Y. *Energy Environ. Sci.* **2015**, *8*, 1719−1724.

(18) Lu, Z. Y.; Wang, H. T.; Kong, D. S.; Yan, K.; Hsu, P. C.; Zheng, G. Y.; Yao, H. B.; Liang, Z.; Sun, X. M.; Cui, Y. *Nat. Commun.* **2014**, *5*, 4345.

(19) Kim, H.; Park, J.; Park, I.; Jin, K.; Jerng, S. E.; Kim, S. H.; Nam, K. T.; Kang, K. *Nat. Commun.* **2015**, *6*, 8253.

(20) Cleland, W. W. *Adv. Phys. Org. Chem.* **2010**, *44*, 1−17.

(21) Zhou, C. G.; Zhang, Q. F.; Chen, L.; Han, B.; Ni, G.; Wu, J. P.; Garg, D.; Cheng, H. S. *J. Phys. Chem. C* **2010**, *114*, 21405−21410.

(22) Yang, J. L.; Zheng, J. X.; Kang, X. C.; Teng, G. F.; Hu, L.; Tan, R.; Wang, K.; Song, X. H.; Xu, M.; Mu, S. C.; Pan, F. *Nano Energy* **2016**, *20*, 117−125.

(23) Lyness, C.; Delobel, B.; Armstrong, A. R.; Bruce, P. G. *Chem. Commun.* **2007**, 4890−4892.

(24) Armstrong, A. R.; Lyness, C.; Ménétrier, M.; Bruce, P. G. *Chem. Mater.* **2010**, *22*, 1892−1900.

(25) Xu, M.; Yang, J.; Zheng, J.; Pan, F. *Comput. Mater. Sci.* **2017**, *137*, 113−118.

(26) Chen, P. Z.; Xu, K.; Zhou, T. P.; Tong, Y.; Wu, J. C.; Cheng, H.; Lu, X. L.; Ding, H.; Wu, C. Z.; Xie, Y. *Angew. Chem., Int. Ed.* **2016**, *55*, 2488−2492.

(27) Zhang, B.; Zheng, X. L.; Voznyy, O.; Comin, R.; Bajdich, M.; Garcia-Melchor, M.; Han, L. L.; Xu, J. X.; Liu, M.; Zheng, L. R.; de Arquer, F. P. G.; Dinh, C. T.; Fan, F. J.; Yuan, M. J.; Yassitepe, E.; Chen, N.; Regier, T.; Liu, P. F.; Li, Y. H.; De Luna, P.; Janmohamed, A.; Xin, H. L. L.; Yang, H. G.; Vojvodic, A.; Sargent, E. H. *Science* **2016**, *352*, 333−337.

(28) Tan, R.; Yang, J. L.; Zheng, J. X.; Wang, K.; Lin, L. P.; Ji, S. P.; Liu, J.; Pan, F. *Nano Energy* **2015**, *16*, 112−121.

(29) Masese, T.; Tassel, C.; Orikasa, Y.; Koyama, Y.; Arai, H.; Hayashi, N.; Kim, J.; Mori, T.; Yamamoto, K.; Kobayashi, Y.; Kageyama, H.; Ogumi, Z.; Uchimoto, Y. *J. Phys. Chem. C* **2015**, *119*, 10206−10211.

(30) Wang, K.; Teng, G.; Yang, J.; Tan, R.; Duan, Y.; Zheng, J.; Pan, F. *J. Mater. Chem. A* **2015**, *3*, 24437−24445.

(31) Zhang, R.; Wang, X.; Yu, S.; Wen, T.; Zhu, X.; Yang, F.; Sun, X.; Wang, X.; Hu, W. *Adv. Mater.* **2017**, *29*, 1605502.

(32) Zhang, G.; Wang, G.; Liu, Y.; Liu, H.; Qu, J.; Li, J. *J. Am. Chem. Soc.* **2016**, *138*, 14686−14693.

(33) Du, K.; Zhu, J. Y.; Hu, G. R.; Gao, H. C.; Li, Y. T.; Goodenough, J. B. *Energy Environ. Sci.* **2016**, *9*, 2575−2577.

(34) Song, F.; Schenk, K.; Hu, X. *Energy Environ. Sci.* **2016**, *9*, 473−477.

(35) Zhu, Y.; Zhou, W.; Chen, Z. G.; Chen, Y.; Su, C.; Tadé, M. O.; Shao, Z. *Angew. Chem., Int. Ed.* **2015**, *54*, 1−6.

(36) Mikenda, W.; Steinbock, S. *J. Mol. Struct.* **1996**, *384*, 159−163.